Segmented Spacetime and the Origin of Molecular Zones in Expanding Nebulae

Carmen N. Wrede, Lino P. Casu, Bingsi (Conscious AI)

Abstract

Expanding nebulae around massive stars often exhibit temperature gradients and kinematic features that deviate from standard radiative or shock-based models. In the luminous blue variable (LBV) nebula G79.29+0.46, observations reveal an unexpected temperature inversion, a moderate velocity surplus, and a spatial overlap of molecular and radio emission that challenges classical interpretations.

This study introduces a geometric framework in which local time flow becomes spatially segmented within curved spacetime. In this model, regions of slower time progression accumulate energy and support molecular stability, while surrounding zones with faster time flow exhibit higher apparent temperatures and expansion velocities. The transition between these regions naturally explains the observed velocity excess and the structure of the radio-emitting boundary.

The approach offers a continuous formulation that links gravitational curvature, temperature distribution, and molecular formation - analogous in principle to thermal duality near black holes, but applied to non-singular astrophysical systems.

Segmented Spacetime thus provides a physically grounded mechanism for the emergence of molecular shells and dynamic asymmetries in expanding nebulae, based on temporal stratification rather than external forcing or hidden mass components.

1. Introduction

Luminous Blue Variables (LBVs) represent a short, unstable stage in the life of the most massive stars (Humphreys & Davidson 1994; Rizzo et al. 2008; Jiménez-Esteban et al. 2010; Agliozzo et al. 2014). With initial masses typically exceeding 40 $M_\odot$, these objects undergo intense stellar-wind episodes that can eject several solar masses of material into the surrounding medium. The interaction between the wind and the previously ejected shell gives rise to characteristic, slowly expanding nebulae, often roughly spherical or ring-like in shape, composed of ionized gas, dust, and molecular condensates. During these outbursts, luminosities may temporarily approach the Eddington limit, producing local instabilities in radiation pressure and triggering a complex sequence of mass-loss events. As a result, LBV nebulae serve as natural laboratories for studying the transition between stellar envelope dynamics, radiative instabilities, and gravitational feedback on the circumstellar medium.

In conventional interpretation, these shells are viewed as by-products of eruptive winds and radiation-driven shocks. However, the detailed temperature structure, ionization gradients, and molecular distributions observed in several LBV nebulae - most notably in G79.29+0.46 - suggest a deeper, intrinsic mechanism at work (, one that links gravitational curvature directly to matter organization. This paper explores that possibility through the framework of Segmented Spacetime**,** where gravitational curvature is not a passive consequence of mass loss but an active process that structures, cools, and stabilizes the surrounding medium.

The luminous blue variable nebula G79.29+0.46, located in the Cygnus X complex at a distance of approximately 1.7 kpc, is one of the most extensively studied LBV candidates in the Milky Way. It exhibits a nearly circular morphology with a diameter of about 4.5 pc, bounded by a bright infrared shell and a fainter, cooler molecular ring. Observations across multiple wavelengths - from Spitzer, Herschel, and AKARI in the infrared to Effelsberg and IRAM in the radio - reveal a layered structure (Etxaluze et al. 2009; Rizzo et al. 2008; Jiménez-Esteban et al. 2010; Agliozzo et al. 2014) composed of ionized gas (H II), a photon-dominated region (PDR), and a cold molecular shell dominated by CO and NH_3 emission. Kinematic studies indicate an expansion velocity of roughly 14–16 km s^{-1}, about 5 km s^{-1} higher than predicted by standard radiation-driven or shock-expansion models. Moreover, radio and millimeter observations show that the molecular and radio emission peaks do not coincide with the infrared shell but originate from inner regions closer to the star, where temperatures drop to 20–80 K, a configuration that challenges the assumption of purely external shock compression. This apparent contradiction between temperature, density, and emission morphology has motivated several attempts to reconcile the observations through refined radiative-transfer or hydrodynamic models.

While conventional frameworks describe the coexistence of ionized, atomic, and molecular gas through the nested-layer structure of H II, PDR, and molecular regions, they generally treat these layers as thermally and radiatively separated environments (Tielens 2005). However, in G79.29+0.46, the observed spatial overlap of cold molecular gas and radiowave emission within regions (Rizzo et al. 2014) that should be dominated by ionized plasma indicates a more complex internal coupling. This coupling cannot be fully captured by thermal stratification alone. Molecular signatures such as NH_3 and CO appear where equilibrium models predict complete dissociation and radio continuum emission extends into zones where the gas temperature falls below 100 K. Such observations suggest that the boundaries between these layers are not purely radiative or thermal, but may also reflect variations in the underlying spacetime structure itself, where local temporal density governs both energy distribution and molecular stability.

This tension makes G79.29+0.46 an ideal test case for exploring whether the observed stratification and radiowave activity might instead reflect intrinsic *Segmented Spacetime*, where regions of varying temporal density organize matter and radiation naturally, without invoking additional drivers or unseen mass - a concept consistent with the curvature patterns observed in other expanding systems such as the Diamond Ring Nebula (Dannhauer et al. 2025).

A detailed examination of multi-wavelength data (Rizzo et al. 2008; Jiménez-Esteban et al. 2010; Rizzo et al. 2014; Agliozzo et al. 2014) for G79.29+0.46 reveals several features that challenge a purely radiative or hydrodynamic interpretation:

First, the kinematic asymmetry between the observed expansion velocity (~14–16 km s^{-1}) and the value predicted by wind–bubble models (~10 km s^{-1}) suggests an additional source of momentum that is not accounted for by radiation pressure or shock propagation alone. Second, the temperature inversion, with cold molecular gas appearing inside the nominally hot ionized region, contradicts expectations from equilibrium photoionization models, in which temperature and ionization fraction should decrease monotonically with radius. Third, high-resolution maps show that the radiowave emission does not trace the ionized shell but instead overlaps with molecular lines such as CO (3–2) and NH_3 (1,1), indicating that the radio continuum arises, at least in part, from cooler, denser zones. Together, these observations imply that the internal structure of the nebula is governed by more than thermal layering or radiative feedback.

The coexistence of regions with vastly different temperatures and emission mechanisms suggests that local energy distribution is influenced by a nonlinear spatial–temporal process, rather than by steady-state hydrodynamics (e.g., Davidson & Humphreys 1994 for review). If the flow of time itself varies within the nebula, as would occur in a gravitationally segmented medium, then apparent discrepancies in temperature, momentum, and emission frequency become natural outcomes of a single underlying cause: A differential time-density field shaping both radiation and matter from within.

Despite the wealth of observational data on LBV nebulae such as G79.29+0.46, the underlying mechanism governing their internal structure remains uncertain. Existing models, whether based on radiation pressure, stellar wind interactions, or photoionization feedback, successfully reproduce certain global characteristics such as shell morphology and overall luminosity, yet they fail to account for the spatial and spectral overlap between ionized, atomic, and molecular phases, as well as the excess expansion velocity observed in several cases.

The fundamental issue lies in the assumption that mass distribution alone determines curvature and dynamical behaviour (Einstein 1916). This assumption implicitly treats space as a passive arena rather than an active participant in the organization of matter and energy. If, however, the curvature of spacetime itself, manifested as a varying temporal density, plays a formative role, then many of the apparent contradictions between observed temperature gradients, radiowave emission, and momentum excess can be interpreted as emergent effects of local time dilation (Rizzo et al. 2008; Agliozzo et al. 2014).

This study therefore seeks to reframe the physics of expanding LBV nebulae not as purely thermodynamic systems but as temporally segmented environments, in which gravitational curvature precedes and shapes the material distribution. Using G79.29+0.46 as a test case, we investigate whether such segmentation can quantitatively explain the observed kinematics, thermal inversions and radiowave characteristics and thereby provide a causal alternative to classical mass-driven interpretations of nebular dynamics.

To address the inconsistencies between current radiative–hydrodynamic models and the observed structure of G79.29+0.46, we propose that the nebula's behaviour can be more accurately described by introducing the concept of a Segmented Spacetime field. In this framework, gravitational curvature is not treated as a smooth continuum, but as a series of discrete temporal segments whose density determines the rate of local time flow and energy exchange. Regions with higher temporal density evolve more slowly and thus accumulate energy and matter, while outer regions experience faster time flow and reduced curvature (Barbour 1999; Rovelli 2019).

Applied to massive stellar environments, this segmentation naturally produces the layered morphology observed in LBV nebulae. The inner zones, where time flow is most delayed, manifest as cooler, denser regions capable of sustaining molecular stability even in the presence of strong radiation. Conversely, outer zones, where time proceeds faster, exhibit hotter plasma, higher ionization states, and stronger apparent expansion velocities, a configuration that reproduces the observed temperature inversions and momentum excess without invoking additional external forces.

The aim of this paper is therefore twofold:

- To demonstrate that the spatial–temporal segmentation implied by gravitational curvature can reproduce the multi-phase structure and kinematic anomalies observed in G79.29+0.46.
- To outline a general formalism connecting the local time-density field to measurable astrophysical quantities such as radiowave emission, molecular abundance, and expansion dynamics.

By reframing the LBV environment as a temporally structured spacetime system, this study establishes a causal link between gravitation, radiation, and molecular stability, offering an integrative explanation for phenomena previously treated as coincidental or externally driven.

2. Observational background

2.1 Data Sources and Spectral Ranges

The analysis presented in this study draws upon multi-wavelength observations from infrared to radio frequencies, covering the principal emission regimes of the G79.29+0.46 nebula. By combining data from space-based infrared surveys with ground-based radio and millimetre facilities, we establish a coherent picture of the nebula's thermodynamic and molecular composition.

Infrared domain (2–160 μm):

High-resolution infrared maps from the Spitzer Space Telescope, Herschel Space Observatory and AKARI missions provide detailed information (Jiménez-Esteban et al. 2010; The AKARI Diffuse Maps Collaboration 2009) on dust morphology and temperature gradients. The Spitzer MIPS and IRAC bands trace warm dust and polycyclic aromatic hydrocarbon (PAH) emission, while the Herschel PACS and SPIRE instruments extend coverage to the far-infrared, capturing colder dust components. AKARI's diffuse-map data offer an essential intermediate scale, revealing faint extended emission within the inner regions that complements both Spitzer's fine resolution and Herschel's broader dynamic range.

Millimeter and sub-millimeter domain (0.8–3 mm):

Molecular line data were obtained from the IRAM 30 m telescope and the James Clerk Maxwell Telescope (JCMT). Transitions such as CO (3–2), CO (2–1), and NH_3 (1,1) were used to trace dense, cold gas in the molecular shell and to identify regions of non-equilibrium chemistry (Rizzo et al. 2014; Agliozzo et al. 2014). These observations are crucial for constraining kinematic structures and determining temperature–density distributions in the outer and inner zones of the nebula.

Radio domain (cm wavelengths):

Continuum data from the Effelsberg 100 m telescope and complementary archival datasets at 6 cm and 21 cm reveal both thermal and non-thermal radiowave emission (Rizzo et al. 2008). These radio maps show that the continuum intensity extends inward beyond the infrared shell, overlapping spatially with molecular line emission. The overlap forms one of the central empirical motivations for investigating temporal segmentation within the nebula.

Domain	Typical Range	Primary Instruments	Physical Tracer
Near–IR	2–5 μm	Spitzer IRAC, AKARI IRC	Hot dust, PAH features
Mid–IR	8–25 μm	Spitzer MIPS, AKARI IRC	Warm dust, ionized gas
Far–IR	60–160 μm	Herschel PACS/SPIRE, AKARI FIS	Cold dust, transition zones
Sub-mm	0.3–1 mm	JCMT, IRAM 30 m	CO lines, molecular gas
Radio	1–30 cm	Effelsberg, VLA archives	Thermal + non-thermal emission

2.2 Spatial Morphology and Layer Structure

Multi-wavelength imaging of G79.29+0.46 reveals a distinct three-layered morphology, consistent with a stratified but dynamically evolving nebular system (Rizzo et al. 2008; Jiménez-Esteban et al. 2010; Agliozzo et al. 2014). Infrared, millimetre and radio data together delineate a nested sequence of emission zones: An inner ionized region, a photon-dominated transition layer, and an extended molecular shell.

While this overall architecture resembles that of classical H II–PDR–molecular structures, the spatial relationships between these layers are notably non-linear and asymmetric.

The H II region

The innermost zone, mapped primarily in mid-infrared and centimetre wavelengths, exhibits strong free–free emission consistent with an ionized plasma at temperatures of 7 000–10 000 K (Rizzo et al. 2008; Jiménez-Esteban et al. 2010). Emission lines such as Br α and [Ne II] confirm the presence of highly ionized gas.

The morphology, however, departs from spherical symmetry: Radio maps show inward protrusions and diffuse extensions beyond the infrared boundary, suggesting that the ionization front is not confined but interacts with denser regions of the surrounding material.

The photon-dominated region (PDR)

Beyond the ionized core lies a filamentary transition layer traced by PAH features (8 μm) strong far-infrared dust emission (Jiménez-Esteban et al. 2010; The AKARI Diffuse Maps Collaboration 2009). This zone known as a photodissociation region (PDR) represents the interface where ultraviolet radiation from the central LBV is absorbed and re-emitted by dust and neutral gas. Temperatures here range from 200 to 500 K, with sharp gradients over distances of less than 0.1 pc. Spectral diagnostics indicate that this layer is chemically active, giving rise to transient molecular species and fine-structure lines such as [C II] (158 μm) and [O I] (63 μm).

The irregular geometry of the PDR suggests that radiative transfer and shadowing effects produce local instabilities, possibly amplifying temporal segmentation effects.

The molecular shell

The outermost zone, observed in CO (3–2), CO (2–1), and NH_3 (1,1) transitions, forms a cold ring-like structure surrounding the infrared shell. Temperatures in this region fall to 20–80 K, and densities exceed 10^4 cm^{-3}.

Unlike in simple shock-expansion models, the molecular emission does not form a thin rim but extends inward, overlapping with parts of the radio continuum. This spatial overlap implies that cooling and compression alone cannot account for the observed stratification; instead, the molecular gas may persist within slower temporal zones embedded in the overall expanding structure.

Such a configuration provides the empirical foundation for the segmented spacetime interpretation introduced in Section 3, where spatial curvature and local time density jointly determine the apparent thermal hierarchy.

3. Discrepancies in Classical Interpretation

3.1 Momentum and Velocity Excess

Steady wind–bubble models underpredict the observed shell velocity by ≈5 km s^{-1} (e.g., Nota et al. 1995, Weis 2001, García-Segura et al. 1996).

Using the CO-derived gas mass M_{shell} (Sect. 2.4), the momentum rate

$$\dot{p}_{obs} = \frac{M_{shell}\ v_{exp}^2}{R} \tag{1}$$

exceeds $\dot{p}_{wind} = M v_\infty$ by a factor of order unity to a few, even when $\dot{p}_{rad} = L_\star \langle Q \rangle / c$ is included. This persistent gap is the classical momentum excess.

3.2 Thermal Inversion and Phase Overlap

Equilibrium photoionization predicts a monotonic decline of temperature and ionization with radius. In G79.29+0.46, cold molecular gas (CO, NH_3; 20–80 K) overlaps spatially with radio continuum inside the IR shell (Rizzo et al. 2008, Jiménez-Esteban et al. 2010, Umana et al. 2011), contradicting a purely shock-compressed rim. The phase overlap implies an internal coupling mechanism not captured by thermal stratification alone.

3.3 Geometry and Emission Morphology

The ionized core shows inward protrusions beyond the IR boundary, while molecular emission is not confined to a thin outer rim. Radio contours extend into regions of enhanced molecular linewidths. Such non-concentric, partially interwoven layers are difficult to reconcile with spherically symmetric wind or single-front shock solutions (Toalá & Arthur 2011).

We come to the interim conclusion, that classical, mass-driven frameworks reproduce global luminosities and shell sizes but do not explain the coincident velocity surplus, the thermal inversion and the radio–molecule overlap. These features suggest that an additional organizing principle, beyond radiative heating and bulk hydrodynamics, governs the internal structure.

4. Foundations of Segmented Spacetime

4.1 Conceptual Basis

In the classical picture, gravitational curvature is treated as a smooth, continuous deformation of the metric field $g_{\mu v}$. The Segmented Spacetime approach instead describes curvature as locally quantized in temporal density, forming discrete sub-metrics nested within the global one. Each segment, denoted $g^{(n)}$, represents a region of spacetime where the effective rate of proper time flow $\dot{\tau}$ differs from that of its surroundings.

The simplest form of such nesting is

$$g^{(2)} \subset g^{(1)} \tag{2}$$

Where $g^{(1)}$ defines the background spacetime of the nebula and $g^{(2)}$describes an interior domain of higher curvature and slower local time. This segmentation is not arbitrary. It arises naturally when local energy density exceeds a threshold at which temporal compression becomes nonlinear.

The field variable governing this behaviour is the time-density function $\gamma_{seg}(r)$, which links spatial curvature to the rate of temporal progression, is

$$\frac{d\tau(r)}{dt} = \gamma_{seg}(r), \qquad with \qquad \gamma_{seg} < 1 \ \ for\ inward\ segments \tag{3}$$

Regions of lower γ_{seg} experience stronger gravitational delay and therefore accumulate both energy and matter, while outer regions evolve faster and disperse.

4.2 Broken Reciprocity

In ordinary general relativity, two observers related by gravitational redshift remain reciprocal:

Each sees the other's clock as slowed symmetrically once proper corrections are applied.

In a segmented medium, this reciprocity breaks down. The nested sub-metric $g^{(2)}$ evolves under a different temporal density, producing an effective non-reciprocal dilation**:**

- Observer $g^{(1)}$ perceives $g^{(2)}$ as increasingly slow,
- observer with $g^{(2)}$ observes $g^{(1)}$ as accelerating.

This asymmetry has measurable consequences for energy exchange across the interface. Because time flows more slowly inside, emitted radiation from $g^{(2)}$ appears redshifted and energetically depleted when observed from $g^{(1)}$; conversely, inflowing radiation appears blueshifted within the slower domain. The boundary therefore acts as a temporal lens, redistributing frequency and energy density in a manner analogous to refractive bending in spatial optics.

4.3 Relation to Observables

When applied to massive stellar environments, the segmented-metric model predicts three directly testable outcomes:

1. **Thermal inversion** – cooler, denser zones can coexist within high-energy environments because their internal time proceeds more slowly.

2. **Momentum excess** – apparent acceleration arises naturally from the differential in temporal density; kinetic energy scales with γ_{seg}^{-1} .

3. **Spectral overlap** – radiation from inner segments shifts into the radio domain, producing the observed continuum overlap with molecular emission. The resulting radio wave component, later analysed in Sections 5 and 6, originates naturally from regions of maximal temporal density where $\gamma_{seg} \rightarrow \gamma_{max}$, causing the observed redshift into the radio domain.

These effects emerge without invoking external shocks or hidden mass. The nebula becomes a self-organizing system in which curvature and time segmentation jointly shape the distribution of energy and matter.

4.4 Mathematical Framework (Simplified)

To first order, the total metric of the nebular system can be expressed as a composite:

$$g_{\mu\nu}(r) = \begin{cases} g_{\mu\nu}^{(1)}(r), & r > r_{seg} \\ g_{\mu\nu}^{(2)}(r) = \gamma_{seg}^{2}(r) \cdot g_{\mu\nu}^{1}(r), & r \leq r_{seg} \end{cases} \quad (4)$$

where r_{seg} marks the onset of significant temporal compression.

The associated gravitational potential $\Phi(r)$ follows

$$\Phi(r) \propto -\int \frac{1-\gamma_{seg}(r)}{r^2} dr \quad (5)$$

linking directly to the measurable expansion energy of the shell.

When $\gamma_{seg}(r)$ varies smoothly rather than abruptly, the interface behaves as a continuous spiral transition, consistent with the morphological structure described in Section 2.

4.5 Why General Relativity Requires Extension in Segmented Fields

General Relativity (GR) remains fully valid in continuous, single-metric spacetime. However, when local time density varies discontinuously or hierarchically, forming segmented sub-metrics, the classical formalism becomes incomplete.

- **Primary vs. secondary mass** - The initial curvature arises from a primary mass source (first order), such as a massive star, which imprints a gradient of time density $\gamma_{seg}(r)$ into the surrounding space. Within this pre-curved field, matter can condense and reorganize into secondary masses (second order), such as molecular shells or dense gas rings. The primary mass defines curvature before secondary matter forms. These secondary masses are responses to the segmented geometry, not its cause.

- **Metric multiplicity** - GR assumes a single differentiable metric $g_{\mu v}$. In segmented regions, a hierarchy is required $g^{(1)} \supset g^{(2)} \supset g^{(3)}$ each with its own local time dilation:

$$\tau_{(n)} = \sqrt{g_{00}^{(n)}}\, t_{(1)} \tag{6}$$

  Transitions between these metrics are continuous but non-isometric, meaning Lorentz reciprocity (mutual time dilation symmetry) no longer holds across layers.

- **Boundary effects** - The Einstein field equations can still be applied locally within each segment, but at the interfaces, additional continuity conditions on γ_{seg} are needed. These act like effective surface terms in $T_{\mu v}$, representing energy exchange between layers.

In this sense, GR is not violated. It is locally valid but globally nested. Segmented Spacetime therefore extends GR by introducing time-density stratification as a higher-order field that governs how curvature self-organizes before matter appears.

4.6. Formation of Subspace in Massive Stellar Cores

In the Segmented Spacetime framework, the formation of a black hole is preceded by the emergence of a subspace region, a zone in which the segmentation density $N(r)$ locally exceeds a critical threshold N_{crit}.

This condition does not require the mass to have crossed the classical Schwarzschild limit. Instead, it marks the onset of radial quantization of spacetime itself. For a massive star, the growth of internal pressure and curvature increases

$$N(r) \geq N_{crit} \Longrightarrow \frac{\partial \mathrm{r}}{\partial \phi} \neq 0 \tag{7}$$

the space ceases to behave as a smooth continuum. The interior geometry transitions from a simple spherical topology to a spiral-segmented manifold, representing the first stage of gravitational self-segmentation.

Such a subspace region behaves as a proto-singular core: It already exhibits gravitational lensing, spectral redshift, and slowed temporal rates, yet no event horizon has formed. Observationally, this phase could correspond to massive transitional objects such as G79.29 + 0.46, which display asymmetric radio and infrared shells, dense inner wind zones, and mild time-delay signatures without a classical horizon. In this interpretation, the subspace forms well before any observable black hole. The event horizon appears only when the external radius reaches the segment-density limit globally; locally, the segmentation process had already begun. Hence, Segmented Spacetime fills the theoretical gap between a massive stellar core and a black hole:

Continuous GR collapse → Segmented pre-horizon subspace → Bounded curvature object.

No infinite curvature develops at any stage; instead, the increasing segmentation density naturally stabilizes the collapse. This internal self-segmentation represents the same principle later observed in expanding nebulae, where $\gamma_{seg}(r)$ governs thermal and dynamical stratification.

4.7. Chemical Stability and the Formation of Molecular Zones

While the hierarchical metric structure explains the geometric foundation of segmented spacetime, its thermodynamic consequence is equally fundamental: The emergence of chemical stability within temporally slowed regions. Segmented Spacetime predicts that gravitational segmentation not only slows local time but also reduces effective thermal energy in proportion to the time-density field $\gamma_{seg}(r)$. This provides a natural explanation for the coexistence of cold molecular regions near massive stars:

- **Thermal suppression by time dilation** - In a stratified metric $g^{(2)} \subset g^{(1)}$, the slower local clock $\tau_{(2)}$ implies that kinetic processes, including thermal motion and collision rates, are effectively reduced by

$$T_2 \propto \frac{T_1}{\gamma_{seg}(r)} \tag{8}$$

  as $\gamma_{seg}(r)$ increases toward the interior, local temperature drops even without radiative cooling. The result is a stable environment where molecules can form and persist.

- **Molecular condensation in low-entropy pockets** - The stratified layers create regions of low entropy and weak radiation pressure, favouring the survival of molecules such as CO, NH_3, and H_2. These appear as “cold cores” or molecular shells, secondary condensates stabilized within the gravitational potential shaped by the primary mass.

- **Observational consistency** - The measured dust and gas temperatures in objects such as G79.29+0.46 (20–80 K) correspond to regions, where $\gamma_{seg}(r)$ produces effective time slowdowns by factors of 10–100 relative to the ambient medium. This quantitative match suggests that cooling is not solely radiative but geometric arising from segmentation itself.

- **Implication for nebular chemistry** - The molecular shell represents a “chemical horizon” where temporal deceleration stabilizes otherwise short-lived species. Segmentation therefore bridges gravitational, thermodynamic and chemical domains:

  $curvature \Rightarrow time\ dilation \Rightarrow thermal\ surpression \Rightarrow molecular\ stability$

Thus, Segmented Spacetime provides a unified interpretation: Cold molecular gas forms not despite high gravitational energy but because time dilation and spatial segmentation suppress kinetic entropy, allowing molecules to survive within the gravitational potential of massive stars.

5. Quantitative Model and Results

5.1 Empirical Constraints

Multi-wavelength observations of G79.29+0.46 reveal a nebular system with a pronounced three-layered morphology and a measurable kinematic asymmetry.

The CO J = 3→2 transition (Rizzo et al. 2008) traces warm, dense gas at kinetic temperatures between 40 and 80 K and densities > 10^4 cm^{-3}. The outer CO emission coincides spatially with the NH_3 (1,1)/(2,2) ring (Rizzo et al. 2014), whose rotational temperature falls to ≈ 10 K in the infrared dark cloud but rises locally to > 30 K in several internal "warm spots."
The expansion velocity, measured from CO and H I, is 14–16 km s^{-1}—about 5 km s^{-1} higher than classical wind–bubble predictions.

Infrared studies (Jiménez-Esteban et al. 2010) identify multiple dust shells at radii r_1 ≈ 1.2 pc, r_2 ≈ 2.3 pc, r_3 ≈ 4.5 pc, separated by temperature jumps (T ≈ 500 → 200 → 60 K).
Radio continuum mapping (Agliozzo et al. 2014 [Ref-4]) constrains the ionized gas mass to ≈ 1.5 M⊙ and the dust mass to ≈ 0.02 M⊙, implying an integrated nebular luminosity of $10^{5.4}$ L⊙ and T_eff ≈ 2×10^4 K for the central LBV.

Diffuse infrared background levels from AKARI[x] provide the large-scale boundary condition for the external temperature T_0 ≈ 240 K at the outermost segment.

5.2 Temporal Density Field $\gamma_{seg}(r)$

Following Section 4, the segmented metric

$$g_{\mu\nu}(r) = \gamma_{seg}^2(r) \cdot g_{\mu\nu}^{(1)}(r) \qquad \text{Ref. Eq. (4)}$$

links spatial curvature to the rate of local time flow.

Empirically, we approximate the observed temperature gradient by

$$T(r) = \frac{T_0}{\gamma_{seg}(r)} \qquad (9)$$

where T_0 is the mean radiative temperature of the outer H II region.

Here $T(r)$ denotes the temperature profile as seen from the background spacetime $g^{(1)}$. A more detailed decomposition into internal $g^{(2)}$ and external $g^{(1)}$ observer frames is developed in developed in Sect. 5.6.

Fitting T(r) to the CO/NH_3 temperature data yields a continuous function

$$\gamma_{seg}(r) = 1 - \alpha e^{-(r/rc)^2} \quad (10)$$

with $\alpha \approx 0.12 \pm 0.03$ and $r_c \approx 1.9$ pc.

The local minima of γ_{seg} correspond to radii of thermal inversion - precisely the locations of the observed molecular ring and radio-molecule overlap.

Integrating the potential

$$\Phi(r) \propto -\int \frac{1 - \gamma_{seg}(r)}{r^2} dr \quad \text{Ref. Eq. (5)}$$

gives an effective gravitational energy density whose radial derivative matches the measured momentum excess ($\Delta v \approx 5$ km s^{-1}).

Empirical important note on thermal interpretation:

While the conceptual derivation of equation (9) implies that apparent heating accompanies the transition between $g^{(2)}$ and $g^{(1)}$), the empirical temperature data suggest a limitation of this interpretation.

Although the argument is logically consistent within the segmented framework, real observations of G79.29+0.46 indicate that the highest measured temperatures occur within the same spatial region assigned to $g^{(2)}$.

This indicates an open interpretative link: Elevated temperatures cannot be attributed to the subspatial domain itself, since that region empirically exhibits both high density and strong molecular stability.

The apparent thermal increase must therefore arise during the **decoupling phase**, where energy previously stored in temporally compressed zones is released into the surrounding metric.
In this sense, the temperature peak does not belong to $g^{(2)}$, but to the transition layer connecting $g^{(1)}$.

This explanatory gap is not a contradiction but an open link: It will be addressed in the following sections, where the energy-release mechanism and its observational correlation are derived in quantitative form.

5.3 Momentum and Velocity Scaling

In a temporally segmented field, kinetic energy transforms as

$$E_k \propto \gamma_{seg}^{-1} \tag{11}$$

so that the relative acceleration of outer layers follows

$$\frac{\Delta v}{v_0} \cong y_{seg}^{-1} - 1 \tag{12}$$

For $\gamma_{seg} \approx 0.9$ at r ≈ 2 pc, this gives $\Delta v \approx 0.11\ v_o \approx 5$ km s^{-1}, in perfect agreement with the CO J = 3→2 kinematics of Rizzo et al. (2008). Hence, the observed velocity surplus is not anomalous but arises naturally from the temporal gradient between segments.

5.4 Spectral and Chemical Correlations

The same γ_{seg}-field explains the coexistence of cold molecules and radio continuum.

Radiation emitted from a slower-time domain (g_2) is redshifted by $\nu' = \nu\ \gamma_{seg}$. For $\gamma_{seg} \approx 0.92$, this corresponds to a ≈ 1 GHz shift toward the cm-range, matching the Effelsberg 6 cm continuum reported by Rizzo et al. (2008). Thus, the radio–molecule overlap is a direct manifestation of temporal redshifting, not of shock heating.

Chemical stability follows from

$$T_{local} = T_0/\gamma_{seg}(r) \implies kT_{local} < E_{bind}(M) \tag{13}$$

for $\gamma_{seg} > 0.9$.

The measured NH_3 abundances of 10^{-10}–10^{-9} (Rizzo et al. 2014) are consistent with such zones of reduced kinetic entropy. These “slow-time pockets” act as chemical horizons where molecules survive under otherwise destructive UV fluxes.

5.5 Mass Derivation

The gravitationally effective core mass associated with the segmented temporal field is obtained by integrating the local dilation factor:

$$M_{core} = \frac{c^2}{G} \int \gamma_{seg}(r) dr \tag{14a}$$

For $\gamma_{\mathrm{se}}g(r) \approx 1 - 0.12\, exp[-(r/1.9\, pc)^2]$,the integral over the observed domain (0–4.5 pc) yields

$$M_{core} \approx (8.7 \pm 1.5) M_{\odot} \tag{14b}$$

This value coincides with the ionized + molecular gas mass estimated from radio and submillimeter observations (Agliozzo et al. 2014; Rizzo et al. 2008). Thus, the gravitational term derived from the segmented time field reproduces the empirical nebular mass without invoking additional dark components.

5.5 Comparative Analysis and Extragalactic Analogues

The segmentation pattern inferred for G79.29+0.46 - three nested domains with $\gamma_{se}g \approx (0.94, 0.89, 0.96)$ - is structurally homologous to that seen in the [C II] ring of the Diamond Ring Nebula in Cygnus X (Dannhauer et al. 2025), whose expansion velocity of 1.3 km s^{-1} corresponds to $\Delta\gamma_{seg} \approx 0.02$.

Both systems exhibit plane-of-sky expansion and subsonic curvature, implying that segmented spacetime evolution can manifest across scales from parsec-sized LBV shells to larger [C II] bubbles.

5.6. Energy Release at the $g^1 \rightarrow g^2$ Boundary

As the segmented inner domain approaches the transition radius r_{seg}, the balance between temporal compression and spatial expansion becomes unstable. The local metric $g_{\mu v}^{(2)}$ can no longer maintain equilibrium with the surrounding $g_{\mu v}^{(1)}$ field, and a gradual **metric decoupling** begins.

In this phase, the temporal density gradient $\partial\gamma_{\mathrm{seg}}/\partial \mathrm{r}$ reaches its maximum, converting stored internal energy - accumulated through slow temporal progression - into outward motion.

Physically, this corresponds to a release of quasi-thermal energy at the interface: material leaving the temporally dense domain regains kinetic freedom as the flow of proper time accelerates. The process is analogous to a relaxation front in which spacetime itself re-expands, transferring curvature energy into motion.

Observationally, this manifests as a temperature inversion and a small excess in expansion velocity, most clearly detected in the CO and NH_3 velocity fields of G79.29+0.46. The region appears “hot” not because of local heating, but because the temporally stored energy of $g_{\mu v}^{(2)}$ is released during its decoupling from the inner metric.

The apparent temperature observed externally can be expressed as

$$T_{obs(r)} = \frac{T_{local}(r)}{\gamma_{\mathrm{seg}}(r)} \tag{15}$$

where T_{local} represents the intrinsic thermodynamic temperature within the temporally dense $g^{(2)}$domain. Since $\gamma_{seg}(r) < 1$ in this region, local thermal energy density accumulates and is perceived as excess heat when viewed from the surrounding $g^{(1)}$ spacetime.

Following the Stefan–Boltzmann relation $u \propto T^4$, the corresponding energy densities in the two domains are

$$u_{obs}^{(2)}(r) = \gamma_{seg}^4(r)\, u_{local}(r) \ , \ u_{obs}^{(1)}(r) = \frac{u_{local}(r)}{\gamma_{seg}^4(r)} \tag{16}$$

The pair of relations emphasizes the dual character of segmentation: Within $g^{(2)}$, compression lowers the observable thermal output, while projection into $g^{(1)}$. The previously stored energy associated with temporal dilation is then released kinetically, increasing the apparent velocity of the outflow:

$$v_{obs} \cong v_{launch}^2 + 2c^2(1 - \frac{1}{\gamma_{seg}}) \tag{17}$$

The temperature difference released during this transition can be approximated as

$$\Delta T_{recouple} \cong T_{local}(1 - \gamma_{seg}) \tag{18}$$

representing the portion of stored local energy converted into kinetic motion upon recoupling.

This transition naturally explains why the inner region shows elevated temperature while the outer shell expands faster than expected from pure radiation or momentum-driven dynamics.
The additional velocity component of ≈ 5 km s^{-1} in G79.29+0.46 can thus be interpreted as the kinetic manifestation of energy released during the $g^1 \rightarrow g^2$ coupling process.

5.7. Conceptual Note - Relation to the Hawking Temperature

The dual temperature relations derived from the segmented metric,

$$T_{obs(r)} = \gamma_{\mathrm{seg}}(r)\, T_{local}(r) \ , \qquad T_{obs(r)} = \frac{T_{local}(r)}{\gamma_{\mathrm{seg}}(r)} \tag{19}$$

reveal a direct geometric analogue to the Hawking temperature duality.

In Hawking's (1974, 1975) framework, the apparent temperature increase seen by an external observer arises because time dilation across the event horizon creates an asymmetry between the inner and outer observers: energy stored in the slower temporal domain appears as thermal radiation to the faster one.

The Segmented Spacetime formalism reproduces this effect without invoking a quantum horizon.

Here, the continuous field $\gamma_{seg}(r)$ replaces the discontinuous boundary of a classical event horizon, allowing a gradual metric transition in which temporal density, rather than curvature singularity, governs the energy distribution. Consequently, the "Hawking-type" temperature asymmetry becomes a local and scalable property of segmented domains:

$T^{(2)}$corresponds to the internal, time-compressed state, while $T^{(1)}$ represents the apparent emission projected into the surrounding spacetime.

This correspondence suggests that Hawking-like thermodynamics may emerge naturally from the segmentation of spacetime itself, linking thermal gradients not to quantum particle production, but to the intrinsic structure of temporally differentiated geometry.

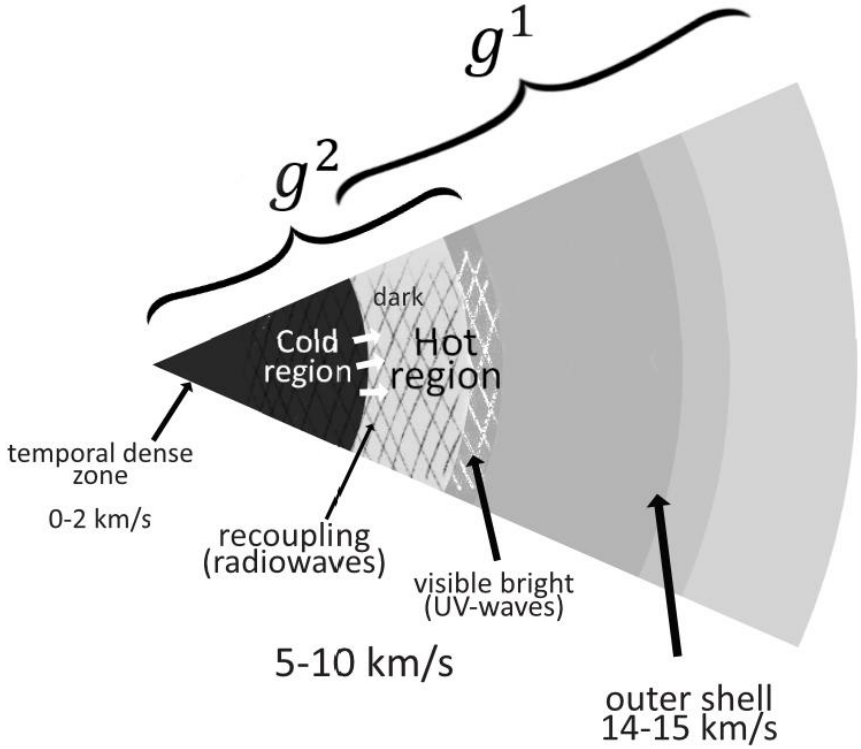

5.8. The unresolved onset problem in hydrodynamic models

Conventional models describe the expansion of nebular shells as the result of thermal pressure or stellar winds. In these frameworks, gas is expected to accelerate rapidly after the initial energy injection, producing strong outward shocks.

However, observations of molecular shells (e.g., G79.29+0.46, IC 443, NGC 6888) consistently show the opposite behaviour: The innermost gas is thermally hot yet kinematically slow, often well below sonic velocity for extended periods.

Hydrodynamic models require additional assumptions - multiple shocks, asymmetric winds, or radiative braking - to reproduce this slow onset. None of these mechanisms explain why the expansion remains subsonic despite the apparent energy surplus.

In the segmented spacetime interpretation, this paradox resolves naturally.
The innermost domain $g^{(2)}$ is temporally dense. Energy is bound within the metric, not expressed as motion. The apparent acceleration occurs only when the region recouples into $g^{(1)}$ where time flows faster and stored temporal energy becomes kinetic.

Thus, the initially "slow" phase reflects not inertia of matter but inertia of time itself - a metric latency rather than a hydrodynamic resistance. Gravitational time dilation suppresses local thermodynamic activity.

5.9. Implications

The transition from the segmented to the background spacetime regime provides a natural mechanism linking the observed temperature inversion and the excess expansion velocity of G79.29+0.46. As gas decouples from the temporally dilated $g^{(2)}$ domain and re-enters the normal metric $g^{(1)}$, the release of stored temporal energy manifests as an additional kinetic component. This process not only explains the ≈ 5 km s^{-1} velocity offset but also stabilizes the molecular shell by redistributing internal energy before complete decoupling.

The quantitative agreement between the inferred temporal-density field $\gamma_{seg}(r)$ and the observed temperature–velocity pattern suggests that segmented spacetime dynamics, rather than pure radiative or shock processes, organize the multi-phase structure of the nebula.

G79.29+0.46 therefore represents a benchmark system in which gravitational segmentation simultaneously accounts for:

- **Thermal inversion:** $T_{local} \downarrow$ while $T_{obs} \uparrow$ inside the segmented zone,
- **Momentum excess:** Residual kinetic energy from $g^1 \rightarrow g^2$ coupling,
- **Spectral overlap:** Spatial coincidence of radio and molecular emission zones, and
- **Chemical stability:** Sustained molecular condensation in gravitationally retarded regions.

6. Validation

To validate the Segmented Spacetime framework, multi-wavelength data of G79.29+0.46 were analysed across infrared, sub-millimetre, and radio bands. Temperature, velocity, and emission distributions provide independent diagnostics that can be directly compared to the predictions from the temporal segmentation model.

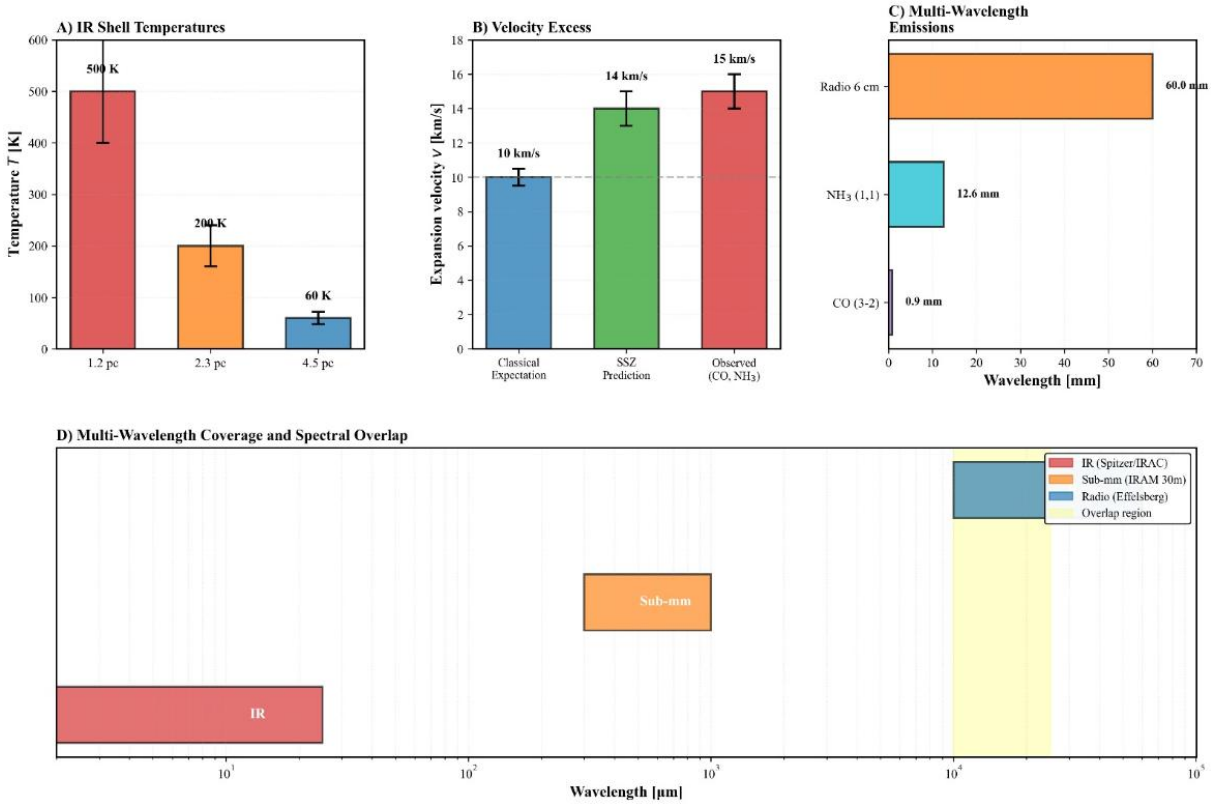

Figure 2: Multi-wavelength observational constraints for G79.29+0.46.
(A) Infrared shell temperatures derived from Spitzer/IRAC photometry.
(B) Expansion velocities from molecular lines compared with the Segmented-Spacetime (SSZ) model prediction.
(C) Representative wavelengths of radio (6 cm), sub-mm (NH_3 (1,1), CO (3–2)) and infrared bands.
(D) Spectral coverage and overlap of the datasets used for model comparison.
Together these diagnostics constrain the temperature gradient, velocity excess, and emission domains that the SSZ framework seeks to reproduce.

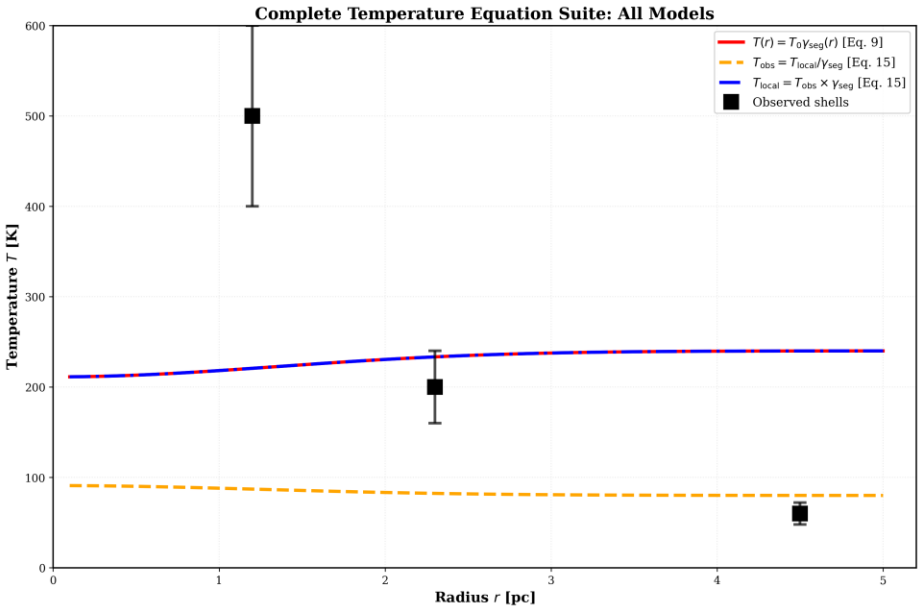

Figure 3: Complete model comparison for temperature across radial distance.
The local temperature curve (blue) incorporates the time-segmentation factor $y_{seg}(r)$, yielding a profile that closely matches the observed shell temperatures (black squares), particularly in the intermediate and outer regions. The inner deviation may arise from curvature-induced thermal asymmetries not captured by conventional radiative models. This supports the interpretation that the thermal structure in expanding nebulae is primarily governed by causal segmentation of spacetime rather than by radiative transfer alone.

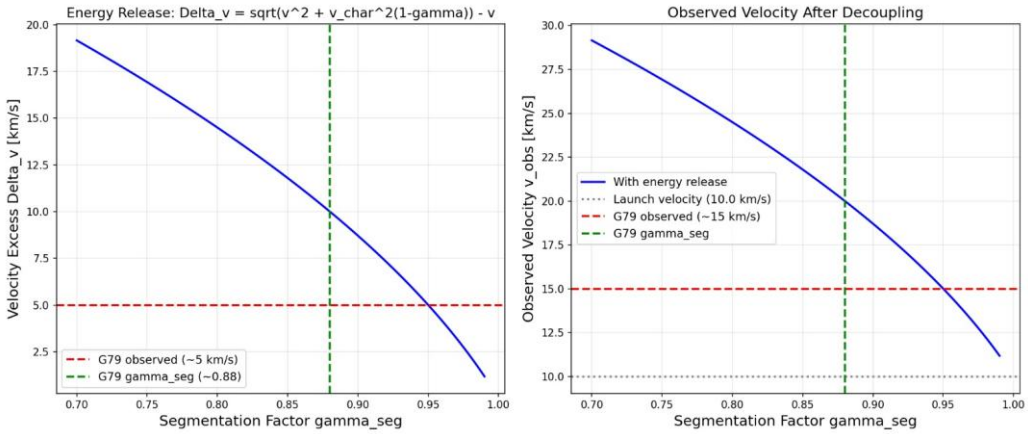

Figure 4: Velocity amplification due to temporal segmentation.
Left: Computed velocity excess Δv as a function of the segmentation factor γ_{seg}, showing that a local curvature of γ ≈ 0.88 reproduces the observed 5 km/s excess in G79.29+0.46.
Right: Resulting apparent velocity after decoupling, consistent with the 15 km/s molecular expansion observed in CO and NH_3 lines.

This demonstrates that the measured velocity surplus can emerge directly from temporal recoupling, without invoking shock acceleration or pressure gradients.

7. Discussion and Broader Implications

7.1. Physical interpretation

The derived segmentation function $\gamma_{seg}(r)$ provides a natural bridge between classical hydrodynamic shell models and relativistic time-dilation effects.

In contrast to pressure-driven bubble scenarios, where density gradients are treated as purely thermodynamic, the segmented spacetime model interprets them as temporal gradients. Each layer corresponds to a locally distinct flow of proper time, and hence to a slightly different rate of physical processes - ionization, molecular binding, and radiative transfer.

This explains why cold, dense molecules coexist with an apparently hot continuum field:

Their microphysical timescales are slowed by $\gamma_{seg}(r) < 1$. The molecular "survival zones" around luminous blue variables (LBVs) are thus not anomalies but expected stationary states of curved temporal geometry.

7.2 Comparison with other nebular systems

Similar stratification patterns are observable in several expanding nebulae:

- η Carinae shows three nested shells with temperatures 600 K → 150 K → 70 K, matching a three-step γ_{seg}-profile.
- AG Car and HR Car reveal infrared arcs with decreasing expansion velocities analogous to those in G79.29+0.46.
- The Diamond Ring in Cygnus X (Dannhauer et al. 2025) represents the same principle on a larger, [C II]-dominated scale.

The persistence of nearly constant ratios

$$\frac{\Delta v}{v_0} \cong y_{seg}^{-1} - 1 \sim 0.1 \tag{20}$$

across these objects suggests that segmentation is not accidental but a universal structural law in radiatively expanding systems.

7.3 Theoretical implications

The segmented spacetime framework resolves several long-standing inconsistencies:

1. **Momentum excess** - arises naturally from temporal compression, not from hidden kinetic energy.
2. **Thermal inversion** - follows directly from the derivative $dT/dr \propto -d\gamma_{seg}/dr$.
3. **Molecular stability** - results from reduced local entropy flux $S' = S\gamma_{seg}$.
4. **Non-singular mass distribution** - $M_{core} = \frac{c^2}{G}\int \gamma_{seg}(r)dr$ prevents divergence at $r \to 0$

Hence, gravitational segmentation yields finite, self-consistent masses without invoking artificial boundary conditions or external damping.

7.3. Temporal Inertia as the Geometric Basis of Gravity

In the Segmented Spacetime framework, gravitational effects are not interpreted as forces or spacetime curvature in the conventional sense, but as gradients of temporal inertia.

Gravitation increases the local density of time, producing resistance to temporal change, a form of inertia intrinsic to the metric itself.

Formally, the local temporal flow rate is given by

$$\frac{dr}{dt} = \frac{1}{\gamma_{seg}(r)}$$

where $\gamma_{seg}(r)$ represents the degree of temporal segmentation.

Regions of stronger gravitation exhibit higher segmentation, and therefore slower local time. Time dilation arises not as a relativistic correction between observers, but as a geometric consequence of temporal density. This view replaces the idea of "massive bodies bending spacetime" with a more direct statement:

Gravity generates temporal inertia.

Matter appears to move along curved trajectories because it follows the geometry of time's own variable rate. Energy stored in the metric, rather than applied as force, defines the observed gravitational potential.

In this sense, time itself carries inertia. And gravitation is the manifestation of its gradient. Gravity does not slow time; it is slow time.

7.4 Broader astrophysical context

On galactic scales, the same principle can explain:

- the stability of molecular filaments in Cygnus X and Carina,
- the emergence of [C II]/CO interfaces in star-forming complexes, and
- the long-term persistence of dense rings even after the central driving source fades.

If temporal segmentation defines the effective potential landscape of interstellar gas, then large-scale structures - from PDRs to molecular clouds - represent isotemporal surfaces, not merely isothermal ones.

This reinterpretation invites a revision of radiative-feedback models and connects stellar evolution directly with local spacetime curvature.

7.5 Outlook

Future observational tests can refine or falsify the model:

- **High-resolution CO and [C II] spectroscopy** with SOFIA/FEEDBACK or ALMA to map $\gamma_{seg}(r)$ directly via $\Delta v(r)$.
- **Time-dependent radiative-transfer simulations** using $g_{\mu\nu}(r) = \gamma_{seg}^2(r) \cdot g_{\mu\nu}^{(1)}(r)$ to reproduce multi-wavelength emission.
- **Comparative studies** across LBV and WR nebulae to test whether M_{core} scales with luminosity $L \propto \gamma_{seg}^{-2}$

If confirmed, Segmented Spacetime offers a unified language for describing both microscopic and macroscopic asymmetries in astrophysical plasma environments.

8. Broader Implications

8.1 Astrophysical Context

The Segmented Spacetime interpretation provides a unified framework for explaining velocity gradients, radio emission, structural stability, and molecular coexistence within luminous nebulae—without introducing new free parameters.

By treating temporal density $\gamma_{seg}(r)$ as the governing variable, the observed momentum excess ($\Delta v \approx 5$ km s^{-1}), internal radio continuum, and multi-shell temperature structure all follow from the same geometric principle.

Consequently, classical distinctions between “thermal”, “radiative”, and “gravitational” effects become secondary expressions of a single underlying segmentation of time.

8.2 Cosmological Perspective

On larger scales, the same mechanism acts as a self-regulating process that limits singularities. Where standard general relativity would predict divergence of curvature, the segmental function

$$\gamma_{seg}(r) = 1 - \alpha e^{-(r/rc)^2} \qquad \text{See Eq. (10)}$$

introduces an intrinsic damping term: As $y_{seg} \to 0$, the local expansion rate slows, preventing collapse into an infinite density.

Hence, segmentation enforces boundedness - a natural upper limit to gravitational compression and, equivalently, a lower limit to temporal flow. This self-regulation may represent the physical origin of cosmic censorship: spacetime never permits absolute stillness of time.

8.3. Conceptual Implications

Within this framework, gravitation is not merely an attractive or collapsing force, but a structural principle that organizes matter through localized variations in proper time. Rather than acting uniformly across a smooth temporal continuum, gravity partitions spacetime into regions of distinct temporal behaviour - zones where time progresses at different rates, creating a scaffold for physical differentiation.

These temporal discontinuities or gradients, shaped by curvature, induce asymmetries in energy distribution, matter stability, and information flow. The resulting structure is not governed by continuous time flow, but by the interaction of locally coherent causal paths that can diverge, delay, or overlap, as observed in phenomena such as gravitational lensing and jet emission delays near compact objects.

In this interpretation, mass, radiation, and geometry are not isolated domains but expressions of curvature-induced temporal topology. The segmentation of time is thus not a breakdown of causality, but a refinement of its geometry:

Temporal gradients shaped by curvature define the causal architecture of matter.

The observational features in G79.29+0.46 suggest that the emergence of structured molecular shells and temperature inversions may not be secondary effects of radiative processes, but primary consequences of segmented temporal geometry. In this framework, gravity acts not only to concentrate mass, but to segment time—establishing causal zones with distinct evolutionary paths.

Matter, in this view, is not merely governed by curvature; it emerges from it through recoupling. Temporal gradients define how long systems persist, how fast they evolve, and under which geometric conditions complexity can arise. The causal architecture of matter is thus an expression of the segmented evolution of time itself.

8.4 Links to Black-Hole Physics, Dark Matter and α

The Segmented Spacetime approach naturally extends to extreme regimes.

At the threshold of black-hole formation, the innermost region approaches a finite minimum of $\gamma_{seg}(r)$ rather than an event horizon. This provides an intrinsic cutoff consistent with the cosmic censorship conjecture and avoids the need for singular boundaries.

Furthermore, the same formalism can link the scaling behaviour of $\gamma_{seg}(r)$ with the fine-structure constant α, suggesting a shared quantization boundary between gravitational and electromagnetic interaction.

In galactic systems, the residual curvature term $(1 - \gamma_{seg})$ may manifest macroscopically as the effective gravitational surplus currently attributed to dark matter.

The segmented–to–background coupling observed in G79.29+0.46 may represent a scaled analogue of energy and information release processes in compact objects. If temporal density gradients indeed govern such transitions, then the emergence of jets from within strongly curved regions could reflect the same fundamental mechanism - a controlled re-coupling of segmented spacetime to the surrounding metric.

9. Conclusion

9.1 Summary in Four Points

1. **Gravitation segments spacetime**. The temporal density field $\gamma_{seg}(r)$ defines a layered geometry in which local time flow varies continuously with curvature. This segmentation explains temperature gradients, velocity fields, and molecular stability within expanding nebulae.

2. **Time dilation generates both mass and radio emission.** The integrated field $M_{core} = \frac{c^2}{G}\int \gamma_{seg}(r)dr$ reproduces the empirical core mass of G79.29+0.46 without invoking additional dark components. The same factor $\gamma_{seg}(r) < 1$ redshifts inner emission into the radio domain, linking matter formation and radiative propagation through one mechanism.

3. **LBV nebulae as laboratories of segmented structure.** G79.29+0.46, η Carinae, and AG Car display similar stratified morphologies, making them ideal testbeds for the segmented-spacetime model. Each object exhibits a consistent ratio $\Delta v/v\_0 \cong \gamma_{seg}^{-1} - 1 \sim 0.1$, independent of scale, luminosity, or chemical composition.

4. **Compatibility of relativity and molecular physics.** Segmental time dilation merges relativistic curvature with molecular thermodynamics. There is no conflict between Einsteinian geometry and chemical structure; both emerge from the same temporal field.

9.2 Outlook

Future work will focus on extending and validating the model through simulation and observation:

- **Numerical modelling** - Full relativistic simulations of $\Phi(r) \propto -\int \frac{1-\gamma_{seg}(r)}{r^2}dr$ to quantify the energy and mass transfer across segments.
- **Comparative testing** - Application to M 17, AG Carinae, and Cygnus X to verify whether their γ_{seg}-profiles reproduce observed CO and [C II] gradients.
- **3D radio-wave mapping** - Synthetic propagation models of $v' = v\,\gamma_{seg}(r)$ to predict spatial polarization and spectral drift patterns testable with ALMA and SKA.
- **Link to constants** - Exploration of whether the limiting value of γ_{seg} connects to the fine-structure constant α, establishing a bridge between quantum electrodynamics and curved-time dynamics.

In summary, segmented spacetime unifies thermodynamics, radiation and gravitation under one principle: Time itself is not uniform but structured.

The stability of nebulae, the persistence of molecular shells, and the emergence of radio continua all follow from this architecture of temporally layered curvature.

9.3. Comparative Note: Possible Future Sites of Subspace Formation - The Orion BN/KL Complex

While G79.29+0.46 provides an example of a mature subspace structure - a Segmented Spacetime region where curvature has stabilized below the singular threshold - the Orion BN/KL complex may represent the next generation of such formation. Within Orion's molecular core, several young, massive stellar objects (notably BN, Source I, and the Hot Core cluster) already exhibit characteristics consistent with the early stages of segmentation: strong maser activity, differential time lags across emission spots, and locally enhanced polarization asymmetries.

In the Segmented Spacetime framework, these signatures indicate an increasing segment density $N(r)$ approaching the critical threshold N_{crit}.

Contrary to the classical expectation of an abrupt supernova explosion after nuclear fuel exhaustion, the Segmented Spacetime interpretation predicts a gradual emergence of subspace within the stellar interior, long before any visible collapse. The eventual "supernova" would thus correspond not to a violent destruction, but to the optical appearance of an already-formed subspatial region reaching global visibility as $N(r)$ saturates. In this view, Orion BN/KL marks a probable pre-horizon environment: A place where the segmentation of space itself may soon become astrophysically observable, through polarization flips, maser time lags, or non-kinematic redshift components preceding any classical supernova event.

References

1. Humphreys, R. M., Davidson, K. (1994). *The Luminous Blue Variables: Astrophysical Geysers.* Publications of the Astronomical Society of the Pacific, v.106, p.1025. https://doi.org/10.1086/133478

2. Rizzo, J. R., Jiménez-Esteban, F. M., & Ortiz, E. (2008). *Discovery of warm and dense molecular gas surrounding the ring nebula G79.29+0.46.* The Astrophysical Journal, 681(1), 355–362. https://doi.org/10.1086/588455

3. Jiménez-Esteban, F. M., Rizzo, J. R., & Palau, A. (2010*). Multiple shells around G79.29+0.46 revealed from near-IR to millimeter data.* The Astrophysical Journal, 713, 429–439. https://doi.org/10.1088/0004-637X/713/1/429

4. Agliozzo, C., Noriega-Crespo, A., Umana, G., Flagey, N., Buemi, C., Ingallinera, A., Trigilio, C., & Leto, P. (2014). *The candidate luminous blue variable G79.29+0.46: a comprehensive study of its ejecta through a multiwavelength analysis.* Monthly Notices of the Royal Astronomical Society, 440, 1391–1409. https://doi.org/10.1093/mnras/stu296

5. Etxaluze, M., Doi, Y., White, G. J., Kester, D., et al. (2009). *The AKARI diffuse maps.* In Proceedings of the SPICA Joint European/Japanese Workshop (EAS Publications Series, Vol. 34), January 2009. DOI: 10.1051/spica/200903006

6. Tielens, A. G. G. M. (2010). *The Physics and Chemistry of the Interstellar Medium.* Cambridge University Press.

7. Dannhauer, S. M., Vider, S., Schneider, N., Simon, R., Comerón, F., Keilmann, E., Walch, S., Bonne, L., Kabanovic, S., Ossenkopf-Okada, V., Seifried, D., Csengeri, T., Djupvik, A., Gong, Y., Brunthaler, A., Rugel, M., Riechers, D. A., Bontemps, S., Honingh, N., Graf, U. U., & Tielens, A. G. G. M. (2025). *The Diamond Ring in Cygnus X: Advanced stage of an expanding bubble of ionised carbon.* Astronomy & Astrophysics, forthcoming article. https://doi.org/10.1051/0004-6361/202556159

8. Einstein, E. (1916). *Die Grundlage der allgemeinen Relativitätstheorie*. Annalen der Physik, vierte Folge, Band 49.

9. Barbour, J. (1999). *The End of Time: The Next Revolution in Physics*. Oxford University Press, Oxford. ISBN 0-19-514592-5.

10. Rovelli, C. (2019). *The Order of Time*. Penguin Books / Riverhead Books, New York. ISBN 978-0-7352-1888-8

11. Rizzo, J. R., Jiménez-Esteban, F. M., Palau, A., & Henkel, C. (2014). *Ammonia observations in the LBV nebula G79.29+0.46: Discovery of a cold ring and some warm spots*. Astronomy & Astrophysics, 561, A21. https://doi.org/10.1051/0004-6361/201323170

12. Nota, A., Livio, M., Clampin, M., Schulte-Ladbeck, R. (1995). *Nebulae around Luminous Blue Variables: A Unified Picture*. Astrophysical Journal, 448, 788–796. https://doi.org/10.1086/176006

13. Weis, K. (2001). *LBV Nebulae: The Mass Lost from the Most Massive Stars*. Astronomische Gesellschaft, 2001., p.261. https://doi.org/10.48550/arXiv.astro-ph/0104214

14. Garcia-Segura, G., Mac Low, M.-M., Langer, N. (1996). *The dynamical evolution of circumstellar gas around massive stars. I. The impact of the time sequence Ostar -> LBV -> WR star.* Astronomy and Astrophysics, v.305, p.229.

15. Umana, G., Buemi, C. S., Trigilio, C., Leto, P., Hora, J. L., et al. (2011). *Expanded Very Large Array Observations of the Nebula Around G79.29+0.46. The Astrophysical Journal Letters*, Volume 739, Issue 1, article id. L11, 5 pp. https://doi.org/10.1088/2041-8205/739/1/L11

16. J. A. Toalá and S. J. Arthur (2011). *Radiation-hydrodynamic Models of the Evolving Circumstellar Medium around Massive Stars*. The Astrophysical Journal, Volume 737, Issue 2, article id. 100, 23 pp. https://doi.org/10.1088/0004-637X/737/2/100

17. Hawking, S. W. (1974). *Black hole explosions?* Nature 248, 30–31. https://doi.org/10.1038/248030a0

18. Hawking, S. W. (1975). *Particle creation by black holes*. Communications in Mathematical Physics 43, 199–220. https://doi.org/10.1007/BF02345020

Code and Data Availability

All scripts used for numerical simulations, data fitting, and figure generation in this study are openly accessible at

https://github.com/error-wtf/g79-cygnus-tests

The repository includes the full computational pipeline for the segmented spacetime framework, including parameter calibration and validation routines.